

# Spin-spin correlations of the spin-ladder compound $(\text{C}_5\text{H}_{12}\text{N})_2\text{CuBr}_4$ measured by magnetostriction and comparison to Quantum Monte Carlo results

Fabrizio Anfuso, Markus Garst, and Achim Rosch

*Institut für Theoretische Physik, Universität zu Köln, Zùlpicher Str. 77, 50937 Köln, Germany*

Oliver Heyer and Thomas Lorenz

*II. Physikalisches Institut, Universität zu Köln, Zùlpicher Str. 77, 50937 Köln, Germany*

Christian Rüegg

*London Centre for Nanotechnology and Department of Physics and Astronomy,  
University College London, London WC1E 6BT, United Kingdom*

Karl Krämer

*Department of Chemistry and Biochemistry, University of Bern, Freiestrasse, CH-3000 Bern 9, Switzerland*

(Dated: March 7, 2008)

Magnetostriction and thermal expansion of the spin-ladder compound piperidinium copper bromide  $(\text{C}_5\text{H}_{12}\text{N})_2\text{CuBr}_4$  are analyzed in detail. We find perfect agreement between experiments and the theory of a two-leg spin ladder Hamiltonian for more than a decade in temperature and in a wide range of magnetic fields. Relating the magnetostriction along different crystallographic directions to two static spin-spin correlation functions, which we compute with Quantum Monte Carlo, allows us to reconstruct the magnetoelastic couplings of  $(\text{C}_5\text{H}_{12}\text{N})_2\text{CuBr}_4$ . We especially focus on the quantum critical behavior near the two critical magnetic fields  $H_{c1}$  and  $H_{c2}$ , which is characterized by strong singularities rooted in the low dimensionality of the critical spin-system. Extending our discussion in Lorenz *et al.* [Phys. Rev. Lett., **100**, 067208 (2008)], we show explicitly that the thermal expansion near the upper critical field  $H_{c2}$  is quantitatively described by a parameter-free theory of one-dimensional, non-relativistic Fermions. We also point out that there exists a singular quantum critical correction to the elastic moduli. This correction is proportional to the magnetic susceptibility  $\chi$  which diverges as  $\chi \sim 1/\sqrt{T}$  at the critical fields and thus leads to a strong softening of the crystal.

## I. INTRODUCTION

By now, the field-induced Bose-Einstein condensation of magnons<sup>1,2</sup> and its one-dimensional analog<sup>3,4</sup> have been observed in many different spin compounds<sup>5</sup> like coupled spin-dimer systems,<sup>6,7,8</sup> arrays of coupled spin-1 chains<sup>9,10</sup> or spin ladders.<sup>11,12</sup> Typically, the ground state of these systems is a spin singlet, separated by a finite energy gap from the lowest triplet excitation. Increasing the magnetic field, two quantum phase transitions are induced. There is a first quantum critical point at a field  $H_{c1}$  where the spin gap closes, and a second at  $H_{c2} > H_{c1}$ , when the fully field-polarized state becomes the exact ground state of the system. The phase between the two critical fields is gapless and, dependent on the dimensionality, is characterized either by long-range order or power-law correlations<sup>4,13</sup> among magnetic moments.

Recently, we have reported in Ref. 14 high-resolution measurements of thermal expansion and magnetostriction of single crystalline piperidinium copper bromide  $(\text{C}_5\text{H}_{12}\text{N})_2\text{CuBr}_4$ . This compound has been previously identified<sup>11</sup> to be a good realization of a two-leg spin ladder. As such, it serves as a perfect model system to test experimentally the validity and applicability of theoretical predictions for quantum critical thermodynamics in a controlled fashion. In particular, it has been argued that the thermal expansion,  $\alpha$ , is an especially useful

probe in the presence of pressure coupling to the critical subsystem because  $\alpha$  is then more singular than the specific heat. This results in a divergent Grüneisen parameter close to quantum criticality<sup>8,15,16,17</sup> with an exponent characteristic for the universality class of the transition. Furthermore, as the thermal expansion is given by the entropy derivative with respect to pressure,  $\alpha \propto \partial S/\partial p$ , it should exhibit a characteristic sign change near the quantum phase transition signaling the accumulation of entropy.<sup>18</sup> The experimental check of these predictions in a controlled model system gives important insights about their reliability and applicability in the pursuit of quantum criticality, especially in materials where the nature of the quantum critical point is unknown.<sup>19,20</sup>

In  $(\text{C}_5\text{H}_{12}\text{N})_2\text{CuBr}_4$ , the presence of two adjacent quantum critical points,  $H_{c1}$  and  $H_{c2}$ , indeed leads to a rich structure of sign changes of thermal expansion reflecting the positions of entropy extrema in the phase diagram. As illustrated in Ref. 14, at low temperatures a maximum in entropy is located near each of the critical fields,  $H_{c1/2}$ , with an enclosed minimum in between. Upon increasing temperature  $T$ , the two maxima approach each other and merge at higher temperatures. Moreover, the low dimensionality of the spin-ladder results in a diverging thermal expansion<sup>14</sup> behaving as  $\alpha \sim 1/\sqrt{T}$  at the two quantum critical points.

The compound  $(\text{C}_5\text{H}_{12}\text{N})_2\text{CuBr}_4$  has a monoclinic

crystal structure ( $\beta \simeq 99.3^\circ$ )<sup>21</sup> with the legs of the spin ladders oriented along the  $a$  axis and the rungs roughly ( $\approx 20^\circ$ ) along the  $c^*$  axis of the reciprocal lattice. The single crystals used for our study have been grown by slow evaporation of a solution of  $(\text{C}_5\text{H}_{12}\text{N})_2\text{CuBr}_4$  in ethanol. Typical crystals grow in plates of several  $mm^3$  with (010) faces and the  $a$  and  $c$  axes oriented parallel to the edges.<sup>22</sup> The measurements have been performed on a home-built capacitance dilatometer in longitudinal magnetic fields up to 17 T for temperatures  $0.3 \text{ K} \lesssim T \lesssim 10 \text{ K}$ . The absence of three-dimensional Néel order in  $(\text{C}_5\text{H}_{12}\text{N})_2\text{CuBr}_4$  down to temperatures  $T_N < 100 \text{ mK}$  implies a very weak inter-ladder coupling giving rise to an extended temperature regime controlled by one-dimensional physics.<sup>22</sup> In this regime, the magnetic subsystem of  $(\text{C}_5\text{H}_{12}\text{N})_2\text{CuBr}_4$  is well-described by the two-leg spin ladder Hamiltonian

$$\mathcal{H} = \sum_{i=1}^N [J_\perp \mathbf{S}_{i,1} \mathbf{S}_{i,2} + J_\parallel (\mathbf{S}_{i,1} \mathbf{S}_{i+1,1} + \mathbf{S}_{i,2} \mathbf{S}_{i+1,2}) - g\mu_B H (S_{i,1}^z + S_{i,2}^z)], \quad (1.1)$$

where the first and second index specify the rung and the chain, respectively. We have identified the exchange couplings to be  $J_\perp/k_B = 12.9 \text{ K}$  and  $J_\parallel/k_B = 3.6 \text{ K}$ , see Sec. II C. The  $g$ -factor is in fact a tensor and so depends on the crystallographic axis along which the magnetic field  $H$  is applied.<sup>21</sup>

In the following, we shortly review the properties of the different ground states of the spin-ladder Hamiltonian (1.1) that appear as a function of magnetic field.<sup>24</sup> At zero magnetic field,  $H = 0$ , the ground state of the spin ladder is a singlet made of short-ranged valence bonds.<sup>25</sup> Due to the dominant rung interaction  $J_\perp/J_\parallel \sim 4$ , these valence bonds can be pictured in a good approximation as the singlet states of the spin dimers located on each rung of the ladder.<sup>26,27,28</sup> The resulting spectrum has a finite gap separating the ground state from the lowest-lying triplet excitations, and, as a consequence, the spin-spin correlations decay exponentially with distance. Upon increasing the magnetic field, this gap decreases until the lowest-lying dispersing triplet excitation touches the singlet energy giving rise to a quantum phase transition at  $H_{c1}$ . For higher fields, singlet and triplet excitations hybridize giving rise to a finite magnetization in the ground state. This phase is a Luttinger liquid and has gapless excitations representing fluctuations of the magnetization perpendicular to the applied magnetic field. Finally, for even higher magnetic fields the zero temperature magnetization saturates above a critical field, i.e. for  $H > H_{c2}$ . Here, the excitations on top of the fully polarized ground state have again a gap that increases with the distance to the transition  $H - H_{c2}$ .

Whereas in Ref. 14 we focused on the thermal expansion and magnetostriction along the  $c^*$  axis of  $(\text{C}_5\text{H}_{12}\text{N})_2\text{CuBr}_4$ , in the present article we also discuss our experimental data measured along the  $a$  and  $b$  axes. Furthermore, we present a detailed comparison with re-

sults of Quantum Monte Carlo (QMC) simulations of the Hamiltonian (1.1) for the full magnetic field range extending beyond the second critical field  $H_{c2}$ . As explained in detail in Sec. II, we numerically evaluate for this analysis spin-spin correlation functions that are related to magnetostriction, as was noted before by Zapf *et al.* in Ref. 29. We find excellent quantitative agreement between theory and experiment that allows to determine the magnetoelastic couplings of  $(\text{C}_5\text{H}_{12}\text{N})_2\text{CuBr}_4$  and their respective uniaxial pressure dependencies. In addition, we present a discussion of the quantum critical thermal expansion near  $H_{c2}$  in Sec. III A. The effective critical theory describing its behavior is known exactly, which enables us to directly calculate the thermal expansion near  $H_{c2}$  without adjustable parameters. Finally, in Sec. III B we note that not only the thermal expansion but also the elastic moduli obtain a quantum critical correction that diverges upon approaching the critical fields. This results in a strong softening of the crystal that finally triggers a first-order transition in the elastic system. We present a mean-field discussion of the phase diagram with the expected position of the line of first-order transitions and the accompanied coexistence regions. Finally, we estimate that this effect is too weak in  $(\text{C}_5\text{H}_{12}\text{N})_2\text{CuBr}_4$  to be observable because the strong one-dimensional signatures will be cut-off by inter-ladder interactions before a first-order transition can develop.

## II. MAGNETOELASTIC COUPLING IN $(\text{C}_5\text{H}_{12}\text{N})_2\text{CuBr}_4$

In the range of temperatures considered here, the main contribution to thermodynamics of  $(\text{C}_5\text{H}_{12}\text{N})_2\text{CuBr}_4$  can be attributed to the spin system, i.e., the spin ladders. As the inter-ladder coupling is sufficiently weak,  $T_N < 100 \text{ mK}$ , it can be neglected, and we can approximate the magnetic part of the free energy,

$$F_m = -k_B T \ln \text{tr} \{ e^{-\hat{H}/k_B T} \}, \quad (2.1)$$

as arising from an ensemble of decoupled spin-ladders. The Hamiltonian thus decomposes into a sum of Hamiltonians,  $\hat{H} = \sum_n \mathcal{H}_n$ , where the index  $n$  counts the number of equivalent ladders in the transverse plane orthogonal to the ladder-leg direction, the  $a$  axis in  $(\text{C}_5\text{H}_{12}\text{N})_2\text{CuBr}_4$ . The Hamiltonian  $\mathcal{H}_n$  represents a single ladder system as defined in (1.1). The free energy density is

$$\frac{1}{V} F_m = \frac{1}{V_D N} \mathcal{F}_m, \quad (2.2)$$

where  $V_D = 859 \text{ \AA}^3$  is the volume per rung,<sup>22</sup> and  $N$  is the number of rungs in the ladder. The free energy  $\mathcal{F}_m$  deriving from a single spin-ladder Hamiltonian  $\mathcal{H}$ , (1.1), is given by  $\mathcal{F}_m = -k_B T \ln \text{tr} \{ e^{-\mathcal{H}/k_B T} \}$ .

The dilatometric properties of  $(\text{C}_5\text{H}_{12}\text{N})_2\text{CuBr}_4$  are characterized by its elastic energy,<sup>23</sup> whose low-temperature and magnetic-field dependencies we expect



FIG. 1: Pictorial representation of the magnetoelastic mode-coupling corrections to the elastic energy, (2.4). The wiggled line represents strain  $u_{ij}$  and the dot is the strain-spin interaction  $g_\alpha$ . The loop of straight lines in diagram (a) represents a two- and in diagram (b) a four-spin correlation function. The tadpole diagram (a) results in a force on the lattice responsible for the magnetostriction and thermal expansion effect. Diagram (b) modifies the elastic tensor.

to be dominated by the spin subsystem. The couplings,  $J_\alpha$ , with  $\alpha = \perp, \parallel$ , of the spin-ladder Hamiltonian (1.1), are determined by the exchange integrals computed from the electronic wavefunctions for given values of lattice parameters. In the presence of strain in the lattice,  $u_{ij}$ , the lattice parameters slightly change and thus induce a variation in the effective couplings,  $J_\alpha = J_\alpha(u_{ij})$ . Expanding this dependence to linear order in the strain,  $J_\alpha(u_{ij}) \approx J_\alpha + g_\alpha^{ij} u_{ij}$ , with  $g_\alpha^{ij} = g_\alpha^{ji} = \partial J_\alpha / \partial u_{ij}|_{u=0}$ , we can separate from (1.1) a magnetoelastic interaction Hamiltonian,

$$\mathcal{H}_{\text{int}} = \sum_{i=1}^N \left[ g_\perp^{nm} \mathbf{S}_{i,1} \mathbf{S}_{i,2} + g_\parallel^{nm} (\mathbf{S}_{i,1} \mathbf{S}_{i+1,1} + \mathbf{S}_{i,2} \mathbf{S}_{i+1,2}) \right] u_{nm}, \quad (2.3)$$

where summation over the indices  $n$  and  $m$  is implied. The strain  $u_{nm}$  fluctuates locally and so depends on the site index  $i$ . The spin-ladder couples linearly to strain and thus acts as a force on the lattice. The lattice responds according to Hooke's law and, as a consequence, inherits the characteristic temperature and magnetic field dependence of the spin-spin correlations in the ladder.

In order to obtain an effective elastic theory, we consider the corrections to the elastic energy density,  $\mathcal{E}$ , in second-order perturbation theory in the magnetoelastic coupling  $g_\alpha$ . Generally, a correction of order  $g_\alpha^n$  to the elastic energy is weighted by a  $2n$ -spin correlation function that can be conveniently represented as an  $n^{\text{th}}$  derivative of the free energy  $F_m$ , Eq. (2.1), with respect to the couplings  $J_\alpha$ ; the most important contributions are illustrated in Fig. 1. The resulting effective elastic energy density reads

$$\mathcal{E}(u) = \frac{1}{2} u_{ij} c_{ijkl} u_{kl} + \frac{1}{V} \frac{\partial F_m}{\partial J_\alpha} g_\alpha^{ij} u_{ij} + \mathcal{O}(g^3). \quad (2.4)$$

The magnetoelastic coupling gives a contribution linear in strain  $u_{ij}$  represented by the tadpole diagram (a) of Fig. 1. The derivative  $\partial F_m / \partial J_\alpha$  acts on the lattice as a  $H$  and  $T$  dependent force that will lead to magnetostriction and thermal expansion. In addition, the elastic tensor obtains a correction that is second order in the interac-

tion  $g$ , see Fig. 1b

$$c_{ijkl} = c_{ijkl}^0 + \frac{1}{V} \frac{\partial^2 F_m}{\partial J_\alpha \partial J_\beta} g_\alpha^{ij} g_\beta^{kl}. \quad (2.5)$$

The tensor  $c_{ijkl}^0$  characterizes the elasticity of the crystal in the absence of spin-strain coupling. Typically, the magnetoelastic coupling  $g_\alpha$  is small and the second-order correction in (2.5) can be neglected. In the following, we will therefore treat the elastic tensor  $c_{ijkl}$  as independent of magnetic field and temperature. As we will discuss in Sec. IIIB, this assumption is very well justified in the temperature range of the experimental data that we present below. Only very close to the quantum critical points,  $H_{c1/c2}$ , the tensor  $c_{ijkl}$  obtains a strong dependence on  $H$  and  $T$  as the second-order derivatives  $\partial^2 F_m / \partial J_\alpha \partial J_\beta$  diverge, resulting in a pronounced softening of the crystal.

Treating the effective elastic theory (2.4) on a mean-field level, we can minimize the elastic energy (2.4),  $\partial \mathcal{E} / \partial u_{ij} = 0$ , to obtain the strain

$$u_{ij} = -(c^{-1})_{ijkl} \frac{1}{V} \frac{\partial F_m}{\partial J_\alpha} g_\alpha^{kl} = \mathcal{S}_\alpha \gamma_\alpha^{ij}, \quad (2.6)$$

where we made use of the inverse of the elastic tensor,  $(c^{-1})_{ijkl} c_{klmn} = \frac{1}{2} (\delta_{in} \delta_{jm} + \delta_{im} \delta_{jn})$ . For later convenience, we also introduced the dimensionless constants

$$\gamma_\alpha^{ij} = -(c^{-1})_{ijkl} \frac{1}{V_D} g_\alpha^{kl} = - (c^{-1})_{ijkl} \frac{1}{V_D} \frac{\partial J_\alpha}{\partial u_{kl}} \Big|_{u=0} \quad (2.7)$$

that quantify the strain dependence of the exchange energies;  $V_D$  is again the volume per rung. Moreover, we defined

$$\mathcal{S}_\alpha = \frac{V_D}{V} \frac{\partial F_m}{\partial J_\alpha} = \frac{1}{N} \frac{\partial \mathcal{F}_m}{\partial J_\alpha}, \quad (2.8)$$

see Eq. (2.2). These quantities can be identified with the spin-spin correlation functions along the rung and along the leg of the ladder,  $\alpha = \perp, \parallel$ ,

$$\mathcal{S}_\perp(T, h) = \frac{1}{N} \sum_i^N \langle \mathbf{S}_{i,1} \mathbf{S}_{i,2} \rangle_{\mathcal{H}} \quad (2.9a)$$

$$\mathcal{S}_\parallel(T, h) = \frac{1}{N} \sum_i^N \langle \mathbf{S}_{i,1} \mathbf{S}_{i+1,1} + \mathbf{S}_{i,2} \mathbf{S}_{i+1,2} \rangle_{\mathcal{H}}, \quad (2.9b)$$

where  $\langle \hat{O} \rangle_{\mathcal{H}} = \text{tr}\{\hat{O} e^{-\mathcal{H}/k_B T}\} / \text{tr}\{e^{-\mathcal{H}/k_B T}\}$ . They depend on temperature,  $T$ , and magnetic field,  $H$ ; the dependence on the latter only enters via the effective field  $h = g \mu_B H$ . These correlators will be basic ingredients in what follows. They determine the  $H$  and  $T$  dependence of the strain due to the magnetoelastic coupling and lead to the magnetostriction and the magnetic contribution to the thermal expansion of  $(\text{C}_5\text{H}_{12}\text{N})_2\text{CuBr}_4$ .

*Uniaxial length changes:* The resulting length change along some axis  $n$  can be obtained by projection of the

strain (2.6),

$$\frac{\delta L_n}{L_n} = \hat{n}_i u_{ij} \hat{n}_j = \mathcal{S}_\perp \gamma_\perp^n + \mathcal{S}_\parallel \gamma_\parallel^n, \quad (2.10)$$

where  $\hat{n}$  is a unit vector along the  $n$  axis. We introduced the abbreviation

$$\gamma_\alpha^n = \hat{n}_i \gamma_\alpha^{ij} \hat{n}_j = -\hat{n}_i \hat{n}_j (c^{-1})_{ijkl} \frac{1}{V_D} \frac{\partial J_\alpha}{\partial u_{kl}} \Big|_{u=0} \quad (2.11)$$

Using  $(c^{-1})_{ijkl} = \partial u_{kl} / \partial \sigma_{ij}$ , with the stress tensor  $\sigma_{ij}$ , we identify the coefficients  $\gamma_\alpha^n$  with the derivatives of the exchange couplings with respect to uniaxial pressure  $p_n$ ,

$$\gamma_\alpha^n = -\hat{n}_i \frac{1}{V_D} \frac{\partial J_\alpha}{\partial \sigma_{ij}} \hat{n}_j = \frac{1}{V_D} \frac{\partial J_\alpha}{\partial p_n}. \quad (2.12)$$

Length measurements on  $(\text{C}_5\text{H}_{12}\text{N})_2\text{CuBr}_4$  were performed along the  $a$ ,  $b$  and  $c^*$  axes. Our detailed comparison between theory and experiment allows us to determine the coefficients  $\gamma_{\perp,\parallel}^n$  for  $n = a, b, c^*$ , which will be given below.

*Magnetostriction:* The magnetostriction is defined as the change of length as a function of magnetic field  $H$

$$\frac{\Delta L_n(T, h_n)}{L_n} \equiv \frac{\delta L_n}{L_n} - \frac{\delta L_n}{L_n} \Big|_{H=0}. \quad (2.13)$$

The magnetostriction depends on the magnetic field,  $H$ , only via the effective field  $h_n = g_n \mu_B H$ . In the present experimental setup the magnetic field has always been aligned parallel to the measured length change such that the  $g$ -factor also carries the same index  $n$ . The  $g$ -factors in the three directions, the  $a$  axis,  $g_a$  (along the legs of the spin ladder), the  $b$  axis,  $g_b$ , and the  $c^*$  axis,  $g_{c^*}$  (roughly along the ladder rungs), of  $(\text{C}_5\text{H}_{12}\text{N})_2\text{CuBr}_4$  were determined in Ref. 21 to

$$g_a = 2.06, \quad g_b = 2.18, \quad g_{c^*} = 2.15. \quad (2.14)$$

The magnetostriction can be expressed in terms of the spin correlators of the ladder,

$$\frac{\Delta L_n(T, h_n)}{L_n} = \gamma_\perp^n \mathcal{D}_\perp(T, h_n) + \gamma_\parallel^n \mathcal{D}_\parallel(T, h_n), \quad (2.15)$$

where we introduced the abbreviation

$$\mathcal{D}_{\perp,\parallel}(T, h) \equiv \mathcal{S}_{\perp,\parallel}(T, h) - \mathcal{S}_{\perp,\parallel}(T, 0). \quad (2.16)$$

Similarly, the derivative of the magnetostriction,

$$\lambda_n(T, h_n) = \frac{1}{L_n} \frac{\partial \delta L_n}{\partial H} = \gamma_\perp^n \frac{\partial \mathcal{S}_\perp}{\partial H} + \gamma_\parallel^n \frac{\partial \mathcal{S}_\parallel}{\partial H}, \quad (2.17)$$

can be decomposed into derivatives of the correlators  $\mathcal{S}_{\perp,\parallel}$ .

*Thermal expansion:* The uniaxial thermal expansion quantifies the length changes of the crystal as a function of temperature at constant magnetic field,

$$\alpha_n(T, h_n) = \frac{1}{L_n} \frac{\partial \delta L_n}{\partial T} \Big|_H = \gamma_\perp^n \frac{\partial \mathcal{S}_\perp}{\partial T} + \gamma_\parallel^n \frac{\partial \mathcal{S}_\parallel}{\partial T}. \quad (2.18)$$

It is determined by the derivatives of the correlators  $\mathcal{S}_{\perp,\parallel}$  with respect to temperature  $T$ .

## A. Experimental results

Uniaxial magnetostriction of  $(\text{C}_5\text{H}_{12}\text{N})_2\text{CuBr}_4$  was measured in a range of temperatures from 0.3 K up to 8 K along the  $a$ ,  $b$  and  $c^*$  axes, see panel (a), (b) and (c), respectively, of Fig. 2. The measurements reveal a rich and complex magnetoelastic behavior. From the low-temperature data, the critical magnetic fields  $H_{c1/2}$  for each direction can be identified by the kinks in the

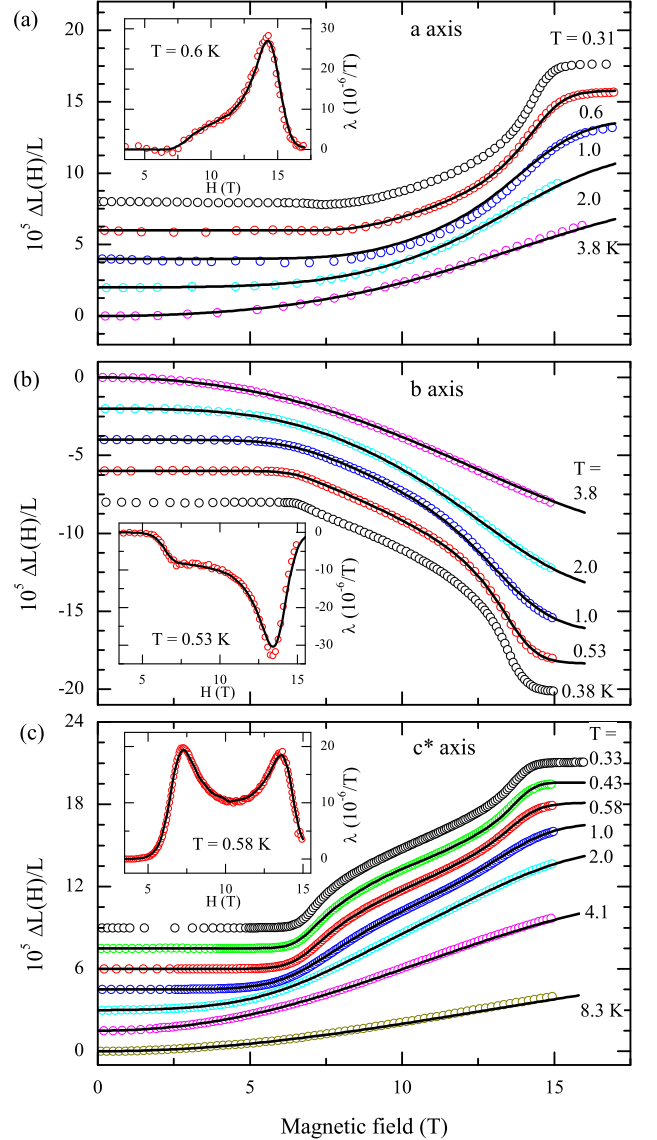


FIG. 2: (color online). The symbols in each panel show the measured magnetostriction  $\Delta L_n/L_n$  of  $(\text{C}_5\text{H}_{12}\text{N})_2\text{CuBr}_4$  along the  $n$  axis with  $n = a, b$ , and  $c^*$  for different temperatures. By construction, the magnetostriction vanishes at  $H = 0$ . The curves at different  $T$  are off-set by  $\pm 2 \cdot 10^{-5}$  in panel (a) and (b), and by  $1.5 \cdot 10^{-5}$  in panel (c). The solid lines are results from QMC simulations. The insets show the fit to the  $\lambda_n$  data from which the  $\gamma$  coefficients in Table I have been determined, see text in Sec. IID.

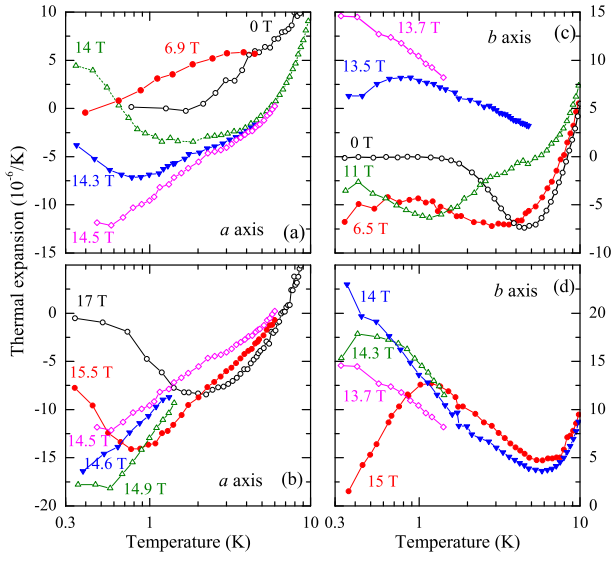


FIG. 3: (color online). Representative measurements of the thermal expansion along the  $a$  axis, i.e. the leg direction (left), and along the  $b$  axis (right) of  $(\text{C}_5\text{H}_{12}\text{N})_2\text{CuBr}_4$ . The upper (lower) panels show data for magnetic fields below (above) the upper critical field  $H_{c2}$ .

magnetostriction. At small fields,  $H < H_{c1}$ , and low temperatures,  $T < J_{\parallel}/k_B$ , the magnetostriction is exponentially small as a consequence of the presence of the spin-triplet gap. Near  $H_{c1}$  the magnetostriction starts to grow and saturates near the second critical field  $H_{c2}$ , becoming  $H$  independent for  $H > H_{c2}$ . For higher temperatures  $T \gtrsim J_{\parallel}/k_B$ , the kinks near the critical fields are smeared out. A saturation plateau at large fields is not reached anymore, and the low-field behavior now becomes quadratic,  $\Delta L_n/L_n \sim H^2$ . The inboxes show the derivatives  $\lambda_n$ , see Eq. (2.17), for  $T \approx 0.58 \text{ K} \ll J_{\parallel}/k_B$ , that exhibit clear anomalies at both critical fields  $H_{c1}$  and  $H_{c2}$ . As discussed already in Ref. 14, at lowest temperature the magnetostriction and  $\lambda_{c^*}$  along the  $c^*$  axis resemble closely the magnetization and susceptibility of  $(\text{C}_5\text{H}_{12}\text{N})_2\text{CuBr}_4$ ,<sup>11</sup> respectively. For the measurements along the  $a$  and  $b$  directions, the shape of the magnetostriction derivative is much less symmetric with respect to  $(H_{c1} + H_{c2})/2$ . In particular,  $\lambda_a$  has only a tiny peak at  $H_{c1}$ . As will be seen below, this is due to the fact that the uniaxial pressure dependence of  $H_{c1}$  almost vanishes for  $a$ -axis pressure  $p_a$  due to a partial cancellation of the uniaxial pressure dependencies of  $J_{\perp}$  and  $J_{\parallel}$ ; see Eq. (2.21) and Table I.

Figure 3 displays some representative data of the thermal expansion measurements along the  $a$  axis (legs) and along the  $b$  axis. For both directions, we find a rich structure in  $\alpha_n$  with various sign changes, similar to our data along the  $c^*$  axis which have been discussed in detail in Ref. 14. Close to  $H_{c2}$  there are again clear indications for a diverging low-temperature thermal expansion for both,  $\alpha_a$  and  $\alpha_b$ . In contrast, however, the features around  $H_{c1}$  are much less pronounced, which is due the afore-

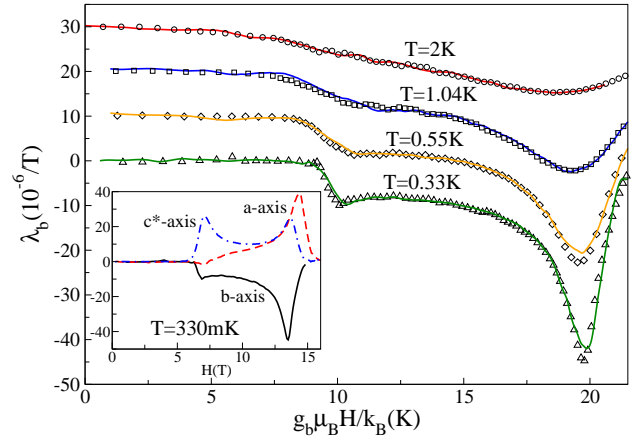


FIG. 4: (color online). Uniaxial magnetostriction along the  $b$  axis,  $\lambda_b$  see Eq. (2.17), of  $(\text{C}_5\text{H}_{12}\text{N})_2\text{CuBr}_4$  at different temperatures (symbols). The higher temperature curves are each offset by additional  $10^{-5}/T$ . The magnetic field is given in units of Kelvin,  $g_b \mu_B H/k_B$ , with a  $g$ -factor along the  $b$  axis  $g_b = 2.18$ . The solid lines are fits using the measurements along the  $c^*$  and  $a$  axes and relation (2.19) with the temperature-independent fitting parameters (2.20). The inset compares the magnetostriction along the three directions at  $T \simeq 330 \text{ mK}$  as a function of the magnetic field  $H$ .

mentioned weak pressure dependencies of  $H_{c1}$  for  $a$ -axis and  $b$ -axis pressure.

## B. Two-parameter scaling

A remarkable prediction of Eq. (2.17) is that the magnetostriction curves along the three directions are linearly dependent. In particular, the magnetostriction in one of the three directions, say, along the  $b$  axis can be obtained as a linear superposition of the other two, along the  $c^*$  and  $a$  axis, i.e. the rung and leg directions, respectively,

$$\lambda_b(T, h) = c_1 \lambda_c(T, h) + c_2 \lambda_a(T, h), \quad (2.19)$$

where  $c_1$  and  $c_2$  are constants independent of temperature and magnetic field. It is important here that one accounts for the  $g$ -factor anisotropy (2.14) by comparing the three measurements at the same effective field  $h = g \mu_B H$ . The sizeable  $g$ -factor anisotropy is reflected e.g. in the slight shift of the positions of the high-field peaks of  $\lambda_n$  for the different field directions, as is illustrated in the inset of Fig. 4.

Fig. 4 confirms that the relation (2.19) is obeyed by the experimental data. The symbols in Fig. 4 show the measurements along the  $b$  axis at different temperatures and the solid line is obtained from the magnetostriction along the  $c^*$  and  $a$  axes and Eq. (2.19) with the fitted values

$$c_1 = -0.36, \quad c_2 = -0.85. \quad (2.20)$$

This agreement serves as an experimental proof that the thermodynamics is fully grasped by a model Hamiltonian with only two pressure-dependent coupling constants.

### C. Determination of the couplings $J_\perp$ and $J_\parallel$

To perform a quantitative comparison of the dilatometric experimental data with theory, we first need to determine the two coupling constants,  $J_\perp$  and  $J_\parallel$ , of the spin-ladder Hamiltonian (1.1). For this purpose, we take the critical fields as an experimental input and derive  $J_\perp$  and  $J_\parallel$  from their second-order strong coupling expressions<sup>31</sup>

$$g\mu_B H_{c1} = J_\perp \left( 1 - \frac{J_\parallel}{J_\perp} + \frac{1}{2} \left( \frac{J_\parallel}{J_\perp} \right)^2 + \mathcal{O} \left( \frac{J_\parallel}{J_\perp} \right)^3 \right), \quad (2.21)$$

$$g\mu_B H_{c2} = J_\perp + 2J_\parallel. \quad (2.22)$$

The formula for  $H_{c2}$  is exact in all orders in  $J_\parallel$ .<sup>26</sup>

To obtain the values of  $H_{c1}$  and  $H_{c2}$  we make use of the temperature scaling of the pronounced peaks near the critical fields in the derivative of the magnetostriction along the  $c^*$  axis,  $\lambda_{c^*}(H)$ , see Fig. 5a. As the temperature is lowered, the peak positions are expected to approach the critical magnetic fields. From the known universality class of the quantum phase transitions, cf. the discussion in Sec. III, we expect the magnetic field value of the peak positions to scale linearly with temperature close to criticality, and this is indeed confirmed by the experimental data as shown in Fig. 5c and d (circles). From the extrapolation we obtain for the critical fields along the  $c^*$  axis,  $H_{c1}^{c^*} = 6.8$  T and  $H_{c2}^{c^*} = 13.9$  T. These values correspond to critical effective fields,  $h_{c1/2} = g_{c^*}\mu_B H_{c1/2}^{c^*}$ ,

$$h_{c1}/k_B = 9.8 \text{ K}, \quad h_{c2}/k_B = 20.1 \text{ K}. \quad (2.23)$$

The measurements along  $a$  and  $b$  yield practically (within 0.1 K) the same value for  $h_{c2}$ , but due to the small peaks around  $H_{c1}$  they do not allow for a reliable quantitative determination of the lower critical fields.

Another feature of the peaks in  $\lambda_{c^*}(H)$  is the steepening of its left and right flank near  $H_{c1}$  and  $H_{c2}$ , respectively, upon lowering  $T$ . As a consequence, two  $\lambda_{c^*}(H)$  measurements closest in temperature show a crossing point on these flanks whose position approaches the critical magnetic fields as the mean of their temperatures vanishes. The extrapolation of the crossing point position confirms the extracted value of  $H_{c1}^{c^*}$  as shown in Fig. 5c (stars). The corresponding test for the  $H_{c2}^{c^*}$  value is not possible due to the enhanced noise in the experimental  $\lambda_{c^*}$  data at higher magnetic fields.

From the critical fields of the  $c^*$ -axis measurements we obtain the coupling constants by using Eqs. (2.21) and (2.22) that are valid up to second order in the small parameter  $J_\parallel/J_\perp$ . We get

$$J_\perp/k_B = 12.9 \text{ K}, \quad J_\parallel/k_B = 3.6 \text{ K}. \quad (2.24)$$

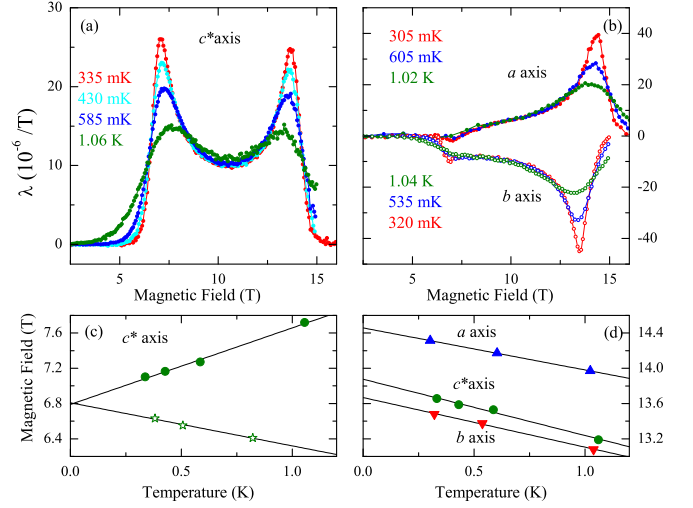


FIG. 5: (color online). The derivatives of the magnetostriction,  $\lambda_n$  of  $(\text{C}_5\text{H}_{12}\text{N})_2\text{CuBr}_4$  measured along  $c^*$  (panel a) and along the  $a$  and  $b$  axis (panel b) for different temperatures. Panel (c) shows the linear- $T$  scaling of the positions of the maxima of  $\lambda_{c^*}$  (dots) and of the crossing points (stars) near  $H_{c1}$  and (d) the positions of the maxima of  $\lambda_n$  near  $H_{c2}$  for the different axes,  $n = a, b, c^*$ ; see text for further explanation.

These values are used for the Quantum Monte Carlo simulations of the spin-ladder Hamiltonian (1.1) presented in the following.

### D. Quantitative comparison of magnetostriction with theory

With the values for the exchange couplings (2.24) the spin-ladder Hamiltonian describing  $(\text{C}_5\text{H}_{12}\text{N})_2\text{CuBr}_4$  is determined. We computed with the Quantum Monte Carlo (QMC) algorithm<sup>30</sup> the spin correlation functions that enter the dilatometric quantities. In Fig. 6 we show the numerically evaluated correlators  $\mathcal{D}_\parallel$  and  $\mathcal{D}_\perp$  of Eq. (2.16) as a function of the effective magnetic field,  $h = g\mu_B H$ , for a series of different temperatures.

The rung correlator  $\mathcal{D}_\perp$  in Fig. 6b increases monotonically with increasing  $h$ . This can be simply understood in the strong-coupling limit,  $J_\perp \gg J_\parallel$ . The rung dimers then form an almost perfect singlet at  $h = 0$  such that a finite magnetic field augments the triplet component to the ground state and thus enhances the ferromagnetic correlations. At low temperatures, the rung correlator  $\mathcal{D}_\perp$  effectively measures the density of triplets and attains a shape very similar to the magnetization curve of the ladder, shown in the inset of Fig. 6b. In zero field,  $h = 0$ , the correlator  $\mathcal{D}_\perp$  vanishes by construction while at  $h \rightarrow \infty$  it saturates to a value close to one. The deviation from one is due to the in-chain quantum fluctuations along the rung. We can obtain the saturation value from the following expansion for the ground state energy per



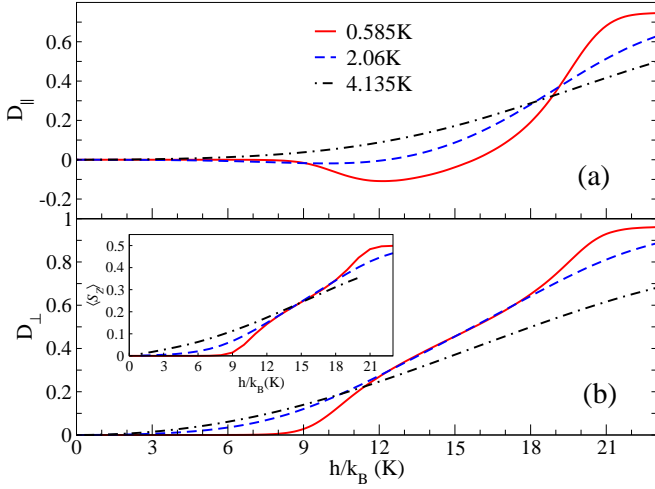


FIG. 6: (color online). Correlators  $\mathcal{D}_{\perp,\parallel}$ , see Eq. (2.16), of the spin ladder Hamiltonian (1.1) with the parameters (2.24), computed with QMC as a function of the effective magnetic field  $h = g\mu_B H$  (in units of Kelvin) for different temperatures. The simulations are performed always in the limit of large number of sites  $N \gg J_{\perp}/(k_B T)$ . The inset shows the magnetization per spin of the ladder. Note the similarity between the rung correlator and the magnetization at low  $T$ .

rung<sup>31</sup>

$$E_0 = -J_{\perp} \left( \frac{3}{4} + \frac{3}{8} \left( \frac{J_{\parallel}}{J_{\perp}} \right)^2 + \frac{3}{16} \left( \frac{J_{\parallel}}{J_{\perp}} \right)^3 + \mathcal{O} \left( \frac{J_{\parallel}}{J_{\perp}} \right)^4 \right). \quad (2.25)$$

For the parameters (2.24) we get for the saturation value

$$\mathcal{D}_{\perp}(0, h)|_{h \rightarrow \infty} = \frac{1}{4} - \frac{\partial E_0}{\partial J_{\perp}} \approx 0.96 \quad (2.26)$$

in agreement with our numerical findings in Fig. 6b.

At low temperatures, the leg correlator  $\mathcal{D}_{\parallel}$  of Fig. 6a is instead a non-monotonic function of the magnetic field. The existence of a minimum can be understood in terms of competing Resonant Valence Bonds.<sup>32</sup> Below the first critical field, the ground state will consist of singlet bonds that for  $J_{\perp} \gg J_{\parallel}$  are mainly formed along the rungs. For  $h \gtrsim h_{c1}$ , the ground state acquires a small triplet component, that is reflected in the presence of rare rung-triplet states. In the presence of these triplets, stronger singlets can be accommodated along the chains enhancing effectively the antiferromagnetic correlations along the legs such that  $\mathcal{D}_{\parallel}$  first decreases. However, increasing  $h$  even further the density of triplets grows, their singlet screening clouds start to overlap, and ferromagnetism finally prevails leading to a sign change in the  $\mathcal{D}_{\parallel}$  function.

The saturation value at  $T = 0$  can again be derived with the help of the ground state energy (2.25),

$$\mathcal{D}_{\parallel}(0, h)|_{h \rightarrow \infty} = \frac{1}{2} - \frac{\partial E_0}{\partial J_{\parallel}} \approx 0.75, \quad (2.27)$$

axis	$\gamma_{\perp}^n \times 10^5$	$\gamma_{\parallel}^n \times 10^5$	$\partial \ln J_{\perp} / \partial p_n$	$\partial \ln J_{\parallel} / \partial p_n$
$a$	4.2	7.7	20%/GPa	133%/GPa
$b$	-8.2	-6.0	-40%/GPa	-104%/GPa
$c^*$	13.5	-1.1	65%/GPa	-19%/GPa

TABLE I: Magnetoelastic couplings  $\gamma_{\alpha}^n = (\partial J_{\alpha} / \partial p_n) / V_D$ , see Eq. (2.12), obtained from a fit of the magnetostriction of  $(\text{C}_5\text{H}_{12}\text{N})_2\text{CuBr}_4$  to the QMC data as shown in Fig. 2, and the resulting uniaxial pressure,  $p_n$ , dependencies of the exchange couplings  $J_{\perp}$  and  $J_{\parallel}$ . The changes of  $J_{\perp}$  and  $J_{\parallel}$  under hydrostatic pressure are given by the respective sums of their uniaxial pressure dependencies.

that coincides with the numerical value in Fig 6a.

In Figs. 2, we show the comparison between the experimentally measured magnetostrictions  $\Delta L_n / L_n$  and the Quantum Monte Carlo data. With the help of the correlators  $\mathcal{D}_{\perp}$  and  $\mathcal{D}_{\parallel}$  computed for  $T = 580$  mK as a function of  $H$  and the relation (2.15), we determine the mixing coefficients,  $\gamma_{\perp}^n$  and  $\gamma_{\parallel}^n$  of Eq. (2.12), by a fit to the experimental data. The resulting values of  $\gamma_{\perp,\parallel}^n$  are listed in Table I. One can check that the coefficients in Table I are consistent with the relation (2.19) using (2.20). Remarkably, these coefficients determined at one temperature yield parameter-free predictions for all the magnetostriction curves measured at other temperatures. As shown in Fig. 2, the agreement between the theory and experiment is perfect in a range of  $T$  of almost one decade. The experimental curves at  $T < 400$  mK have not been calculated because our QMC algorithm could not produce reliable data at such low temperature.

The two correlators  $\mathcal{D}_{\perp,\parallel}$  contribute roughly equally to the magnetostriction along the  $a$  axis (leg direction) and the  $b$  axis; the corresponding ratio of mixing coefficients is of order one. Along the  $c^*$  axis (rung direction), however, the magnetostriction is dominated by  $\mathcal{D}_{\perp}$  except for a small 8% admixture of the leg correlator. This agrees with the naive expectation that squeezing the ladder along the rung mainly affects  $J_{\perp}$ . As a consequence, the magnetostriction  $\Delta L_{c^*} / L_{c^*}$  inherits the characteristic shape of the correlator  $\mathcal{D}_{\perp}$  that resembles at low  $T$  the magnetization of the ladder as a function of  $H$ . This also explains the similarity between the susceptibility<sup>11</sup> of  $(\text{C}_5\text{H}_{12}\text{N})_2\text{CuBr}_4$  and the derivative  $\lambda_{c^*}$ , that shows two characteristic peaks located close to the critical fields  $H_{c1/2}$ . In Ref. 14, we neglected the 8% admixture of the leg correlator and interpreted the thermal expansion data along the  $c^*$  direction solely in terms of a pressure dependence of  $J_{\perp}$ . In this approximation, the thermal expansion  $\alpha_{c^*}$  can be related to the  $H$  derivative of the entropy,  $\alpha_{c^*} \propto \partial S / \partial H$ , that allows to understand in simple terms the various sign changes of thermal expansion.<sup>18</sup>

### III. QUANTUM CRITICALITY

Near the two critical fields,  $H_{c1}$  and  $H_{c2}$ , the lowest-lying triplet excitation or the spin-wave excitation become gapless, respectively. Both transitions are described by a Hamiltonian of free non-relativistic fermions,  $c(x)$ , representing the corresponding excitations<sup>24,33</sup>

$$\mathcal{H}_{\text{cr}} = \int dx c^\dagger(x) \left( -\frac{\hbar^2 \partial_x^2}{2m} + r \right) c(x) \quad (3.1)$$

where the mass  $m$  differs for the two transitions and the control parameter,  $r \propto H - H_{c1/2}$ , measures at  $T = 0$  the distance to the quantum critical point. The resulting critical contribution to the free energy density is

$$f_{\text{cr}}(r, T) = -\frac{a}{V_D} \frac{\sqrt{2m}}{\hbar} (k_B T)^{3/2} \mathcal{F} \left( \frac{r}{k_B T} \right) \quad (3.2)$$

with the volume  $V_D$  per rung and the distance  $a$  between the rungs. The scaling function is given by

$$\mathcal{F}(x) = \int_0^\infty \frac{dy}{\pi} \log [1 + \exp(-y^2 - x)]. \quad (3.3)$$

#### A. Critical thermal expansion near $H_{c2}$

In the following, we will focus on the critical behavior near the upper critical field,  $H_{c2}$ . The ground state of the system for  $H > H_{c2}$  is particularly simple: all spins are fully polarized by the magnetic field. This allows to determine the parameters exactly,<sup>26</sup>

$$m = \frac{\hbar^2}{J_{\parallel} a^2}, \quad r = g\mu_B H - (J_{\perp} + 2J_{\parallel}). \quad (3.4)$$

We will consider the predictions for the uniaxial thermal expansion  $\alpha_n$  and compare it to experiment. The uniaxial length change close to  $H_{c2}$  can be obtained from (2.6) by approximating the magnetic free energy with its critical part,  $F_m/V \approx f_{\text{cr}}$ . Moreover, the dominant contribution originates from the sensitivity of  $f_{\text{cr}}$  upon small variations of the control parameter  $r$  so that we can neglect  $\partial f_{\text{cr}}/\partial m$  as it only gives sub-leading corrections close to the quantum critical point. So we obtain

$$\frac{\delta L_n^{\text{cr}}}{L_n} = -V_D \frac{\partial f_{\text{cr}}}{\partial r} (\gamma_{\perp}^n + 2\gamma_{\parallel}^n). \quad (3.5)$$

From this expression, we derive the critical uniaxial thermal expansion close to  $H_{c2}$ ,  $\alpha_n^{\text{cr}} = (\partial \delta L_n^{\text{cr}}/\partial T)/L_n$ ,

$$\alpha_n^{\text{cr}} = (\gamma_{\perp}^n + 2\gamma_{\parallel}^n) \sqrt{\frac{2k_B}{J_{\parallel} T}} \left[ \frac{1}{2} \mathcal{F}'(x) - x \mathcal{F}''(x) \right]_{x = \frac{r}{k_B T}} \quad (3.6)$$

where the primes indicate derivatives of the function  $\mathcal{F}(x)$ , (3.3). Formula (3.6) is the limiting behavior of

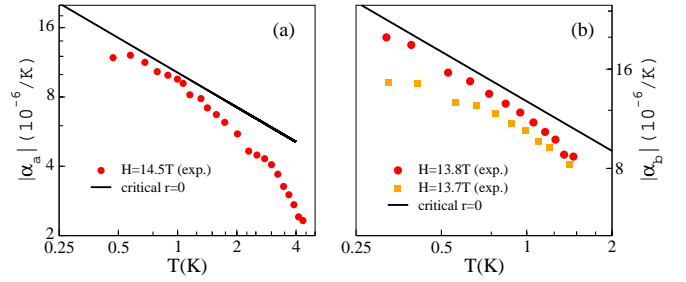


FIG. 7: (color online). Quantum critical thermal expansion near  $H_{c2}$  of  $(\text{C}_5\text{H}_{12}\text{N})_2\text{CuBr}_4$  (symbols) along the  $a$  and  $b$  axis and comparison with the parameter-free theory (3.7) (lines). The critical fields along the three directions as extracted in Fig. 5d are given by  $H_{c2}^a = 14.5$  T and  $H_{c2}^b = 13.7$  T.

thermal expansion near the quantum critical point at  $H_{c2}$ . It is expected to describe asymptotically the experimental data in the range  $|r|/k_B, T \ll J_{\parallel}/k_B = 3.6$  K. At criticality,  $r = 0$ , the thermal expansion diverges with temperature as  $1/\sqrt{T}$ ,<sup>14</sup>

$$\alpha_n^{\text{cr}}|_{H=H_{c2}} = \mathcal{C} (\gamma_{\perp}^n + 2\gamma_{\parallel}^n) \sqrt{\frac{k_B}{J_{\parallel} T}}, \quad (3.7)$$

with the prefactor  $\mathcal{C} = (\sqrt{2} - 1) \zeta(1/2)/(2\sqrt{2\pi}) \approx -0.12066$ . The next-to-leading order correction to the result (3.7) originates from two-magnon scattering processes that lead to a temperature-independent contribution to  $\alpha_n$  at  $H = H_{c2}$ . The strain dependence of the mass  $m$  in (3.4) and higher-order derivatives of the magnon dispersion, on the other hand, yield corrections to (3.7) that are suppressed by a relative factor  $k_B T/J_{\parallel}$ . All these corrections to scaling are neglected in the following.

The mixing coefficients  $\gamma_{\perp, \parallel}^n$  entering (3.6) have been already determined in Sec. II and are listed in Table I. This allows us to perform a parameter-free calculation of  $\alpha_n$  near the quantum critical point at  $H_{c2}$ . Fig. 7 shows a comparison of the uniaxial thermal expansion of  $(\text{C}_5\text{H}_{12}\text{N})_2\text{CuBr}_4$  with formula (3.7) (lines) on a double-logarithmic scale. Note that the critical field  $H_{c2}$  differs for the three crystallographic axes, as it is given by  $H_{c2}^n = h_{c2}/(g_n \mu_B)$  where  $h_{c2}/k_B = 20.1$  K and the  $g$ -factors are listed in Eqs. (2.14). Measurements of  $\alpha_a$  were performed at the critical field  $H_{c2}^a = 14.5$  T and are displayed in Fig. 7a. The data nicely approaches the asymptotic  $1/\sqrt{T}$  behaviour at lowest temperatures. Panel (b) displays  $\alpha_b(T)$  along the  $b$  axis for two fields closest to the critical field. The saturation of the curve at  $H = 13.7$  T at lowest temperatures suggests that the critical field is slightly higher than the value  $H_{c2}^b = 13.7$  T which follows from Eq. (2.23) with  $g$ -factor  $g_b = 2.18$ . The deviation is, however, within the error bar for the critical field value of  $\simeq \pm 0.05$  T associated with the analysis in Fig. 5d. As expected, in both panels the corrections to scaling behaviour of  $\alpha_n$  are still sizeable in the considered temperature range.



### B. First-order transition driven by quantum criticality

The above considerations were based on the assumption made in Sec. II that the elastic tensor (2.5) is independent of magnetic field and temperature and, in particular, is such to ensure the stability of the crystal. Here we show that this assumption breaks down in the immediate vicinity of the quantum critical points of the spin ladder. Close to the quantum phase transition, the spin ladder is described by the Hamiltonian (3.1). Near criticality, the most relevant magnetoelastic interaction derives from the strain dependence of the control parameter  $r$ . As  $r$  is just a certain function of the exchange couplings  $J_\alpha$ , we can repeat the reasoning of Sec. II to derive an effective magnetoelastic interaction Hamiltonian,

$$\mathcal{H}_{\text{int}}^{\text{cr}} = \int dx c^\dagger(x) c(x) g_r^{ij} u_{ij}(x) \quad (3.8)$$

where the coupling  $g_r^{ij} = \partial r / \partial u_{ij}|_{u=0}$  measures the strain dependence of the control parameter. In second-order perturbation theory in  $g$ , this interaction then leads to an effective elastic tensor of the form,

$$c_{ijkl} = c_{ijkl}^0 - \chi_{\text{cr}} g_r^{ij} g_r^{kl}. \quad (3.9)$$

The strong temperature and magnetic field dependence enters via the susceptibility  $\chi_{\text{cr}}$  that is obtained from the critical free energy (3.2)

$$\chi_{\text{cr}} = -\frac{\partial^2 f_{\text{cr}}}{\partial^2 r} = \frac{a}{V_D} \frac{\sqrt{2m}}{\hbar \sqrt{k_B T}} \mathcal{F}'' \left( \frac{r}{k_B T} \right). \quad (3.10)$$

Note that for the spin ladder,  $r \propto H - H_{c1/2}$ , such that  $\chi_{\text{cr}}$  indeed coincides with the critical magnetic susceptibility of the system. Moreover,  $\chi_{\text{cr}}$  is positive so that the magnetoelastic coupling correction in (3.9) reduces the elastic moduli. In fact, the susceptibility  $\chi_{\text{cr}}$  diverges – like the thermal expansion – as  $1/\sqrt{T}$  at criticality,  $r = 0$ , resulting in a strong softening of the crystal until it becomes unstable sufficiently close but still away from the quantum critical point. The lattice is then expected to undergo a first-order transition that preempts quantum criticality.

The singular contribution to the elastic moduli in (3.8) is attributed to the low dimensionality  $d = 1$  of the critical system, i.e., the spin ladder. Generally, in the presence of a strain coupling to the square of the order parameter, a divergent contribution to elasticity is expected when

$$\nu(d+z) < 2, \quad (3.11)$$

where  $\nu$  is the correlation length and  $z$  is the dynamical exponent of the quantum critical point. If this criterion is fulfilled the lattice becomes unstable before the quantum phase transition is reached. The condition (3.11) is related to the corresponding criterion for compressible

classical critical systems.<sup>34,35,36,37</sup> There, it is known that a second-order transition is preempted by an instability of the lattice if the specific heat exponent is positive,  $\alpha = 2 - \nu d > 0$ . From this, the criterion for compressible quantum critical systems (3.11) is obtained by replacing the spatial dimension  $d$  with the effective dimension  $d+z$ .

Compressible critical systems have been studied extensively in the past, see Ref. 38 and references therein. Renormalization group (RG) treatments of such systems yield run-away RG flow that is interpreted as an indicator for a first-order transition. For isotropic media, where the elastic tensor is characterized by just two moduli, compression and shear, this conclusion is borne out by explicit calculations.<sup>37</sup> Interestingly, the arising transition turns out to be governed by long-range interactions and is therefore mean-field like. An analysis of compressible critical models for materials with lower crystal symmetry is in general, however, rather challenging.<sup>38,39,40</sup>

Here, we do not aim for a complete description of a possible first-order transition in the monoclinic crystal structure of  $(\text{C}_5\text{H}_{12}\text{N})_2\text{CuBr}_4$  triggered by quantum critical fluctuations. For an estimate of the location of first-order transitions in the phase diagram, we consider instead the elastic properties on the level of a simplistic mean-field theory. Neglecting phonon excitations and crystal anisotropies, an effective Landau potential for the macroscopic volume change  $u = \Delta V/V$  can be derived

$$\mathcal{V}(u) = \frac{K_{\text{eff}}}{2} u^2 + f_{\text{cr}}(r + gu, T) \quad (3.12)$$

where  $K_{\text{eff}}$  is an effective bulk modulus and with  $f_{\text{cr}}$  given in Eq. (3.2). The first argument of  $f_{\text{cr}}$  is the control parameter expanded in first order in  $u$  with the coupling constant  $g \equiv \partial r / \partial u|_{u=0}$ . For conditions of fixed hydrostatic pressure, minimization of the potential  $\mathcal{V}$  yields the value of volume change  $u_{\text{min}}(r_0, T)$  at given  $r_0$  and temperature  $T$ . At  $r_0 = T = 0$ , the critical part behaves as  $f_{\text{cr}} \sim |u|^{\nu(d+z)} \Theta(-u)$  and dominates over the quadratic part of the potential if the criterion (3.11) is fulfilled; for the spin ladder we have  $\nu(d+z) = 3/2$ . Due to this strong non-analyticity of the Landau potential (3.12) near the apparent quantum critical point, the value of  $u_{\text{min}}$  jumps in its vicinity and thus avoids the strong critical fluctuations by prohibiting the argument  $r_0 + gu_{\text{min}}$  to approach zero.

The resulting line of first-order transitions and the coexistence region in the phase diagram are shown in Fig. 8. The line of first-order transitions terminates in a second-order endpoint, which we numerically evaluated to be located at

$$r^*/\varepsilon_0 = 0.0205 \pm 0.0003, \quad k_B T^*/\varepsilon_0 = 0.0155 \pm 0.0005. \quad (3.13)$$

The characteristic energy scale  $\varepsilon_0 = \frac{g^4 a^2 2m}{V_D^2 K_{\text{eff}}^2 \hbar^2}$  is suppressed by the fourth power of the coupling  $g$  and the temperature  $T^*$  is therefore expected to be small. We expect the second-order transition at the endpoint

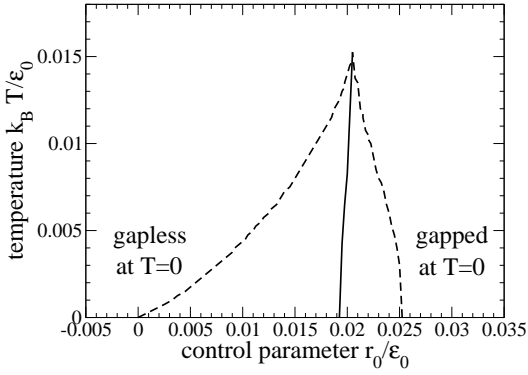


FIG. 8: Phase diagram numerically evaluated from the Landau potential (3.12); temperature and control parameter are given in units of the energy scale  $\varepsilon_0 = \frac{a^4 a^2 m}{V_D^2 K_{\text{eff}}^2 \hbar^2}$ . The first-order transition line (solid) is embedded in a coexistence region which is bounded by the dashed lines; the critical fluctuations at  $T = 0$  are gapped (gapless) on the right (left) hand side of the transition line.

$(r^*, T^*)$  to be particular: generically, it should be mean-field like and as such it is not accompanied by critical fluctuations.<sup>37,40</sup>

In order to get the order of magnitude for the transition temperature  $T^*$  we estimate the energy scale  $\varepsilon_0$  near the critical field  $H_{c2}$  of  $(\text{C}_5\text{H}_{12}\text{N})_2\text{CuBr}_4$ . Away from criticality, the coupling  $g$  obeys  $g = \frac{\partial}{\partial u} r = -K_{\text{eff}} \frac{\partial}{\partial p} r \equiv K_{\text{eff}} V_D \gamma$ ; with the expression for the mass  $m$ , Eq. (3.4), we then obtain  $\varepsilon_0 = \frac{2\gamma^4 V_D^2 K_{\text{eff}}^2}{j_{\parallel}}$ . Using for the modulus the estimate  $K_{\text{eff}} \sim 10$  GPa (assuming a rather soft material) and a  $\gamma$  value,  $\gamma \sim 10^{-4}$ , of the order of the ones in Table I we get the rough estimate  $\varepsilon_0/k_B \sim 10^{-5}$  K. The small numerical prefactor in (3.13) suppresses the critical temperature further by two orders of magnitude,  $T^* \sim 10^{-7}$  K. This small value of  $T^*$  suggests that the phenomenon of fluctuation-induced first-order transitions close to quantum criticality is irrelevant for  $(\text{C}_5\text{H}_{12}\text{N})_2\text{CuBr}_4$  and cannot be observed. In particular, the above discussion applies only in the temperature regime where thermodynamics is dominated by the one-dimensional physics of the spin ladders. At criticality, the inter-ladder coupling  $J_{3d}$  leads to a dimensional crossover at a temperature  $T_{3d}$  from 1d to 3d quantum critical behavior,<sup>2,41</sup> which weakens the non-analyticity in the effective Landau potential for the strain  $u$ , and Eq. (3.12) ceases to be applicable for temperatures  $T \lesssim T_{3d}$ . Moreover, quantum criticality in the 3d regime is not strong enough to have the criterion (3.11) fulfilled. In the framework of the 3d dilute interacting Bose gas with anisotropic hopping,<sup>2</sup> the crossover temperature,  $T_{3d}$ , can be estimated to be of the order of the inter-ladder coupling,  $T_{3d} \sim J_{3d}/k_B$ . From the measured Néel temperature near  $(H_{c1} + H_{c2})/2$ ,  $T_N \simeq 80$  mK,<sup>22</sup> it follows that  $J_{3d}$  is at least three orders of magnitude larger than our estimate of  $T^*$ . This means that in  $(\text{C}_5\text{H}_{12}\text{N})_2\text{CuBr}_4$  the divergent correction to the elastic tensor (3.8) is cut-off by inter-ladder interactions

before any modulus vanishes. Nevertheless, the strong softening of the crystal close to the critical fields should give pronounced signatures, e.g., in ultrasound measurements.

The derivation of the quantum critical correction to the elastic tensor (3.9) was based on very general arguments. In particular, the prediction of the correction being proportional to the magnetic susceptibility  $\chi$  carries over to any magnetic-field driven quantum critical point. Such a correspondence between  $\chi$  and the elastic moduli has been indeed found by Schmidt *et al.*<sup>42</sup> in the spin-dimer system  $\text{NH}_4\text{CuCl}_3$ . This compound exhibits a series of quantum phase transitions as a function of magnetic field that are ascribed to the successive polarization of nearly decoupled spin-dimer subsystems.<sup>43,44</sup>

#### IV. SUMMARY

The magnetostriction and thermal expansion of  $(\text{C}_5\text{H}_{12}\text{N})_2\text{CuBr}_4$  are described to a remarkable level of accuracy by the two-leg spin-ladder Hamiltonian of Eq. (1.1), with the two exchange couplings  $J_{\perp}$  and  $J_{\parallel}$  given in Eq. (2.24). The presence of only two characteristic energy scales leads to an interdependence of the magnetostriction measured along different crystallographic directions. This predicted dependence is confirmed by the experiments, as shown in Fig. 4, and justifies<sup>11</sup> the disregard of other possible terms in the Hamiltonian, e.g. diagonal or ring exchange couplings. As a consequence, the contribution of the spin subsystem to the elastic properties are captured by two static nearest-neighbor spin-spin correlation functions,<sup>29</sup> which we calculated numerically with QMC. Their contribution to magnetostriction along some arbitrary axis  $n$  is weighted by effective magnetoelastic coupling constants that we denoted by  $\gamma_{\perp, \parallel}^n$ , see Eq. (2.12). A detailed fit to the experimental magnetostriction data, see Fig. 2, allowed us to determine these coupling coefficients for the three crystallographic directions  $a$ ,  $b$  and  $c^*$  of  $(\text{C}_5\text{H}_{12}\text{N})_2\text{CuBr}_4$ . Their values are given in Table I.

In particular, we find that along the rungs of the ladder, i.e. the  $c^*$  axis, the magnetostriction is dominated by the strain dependence of the rung coupling  $J_{\perp}$ . This explains the resemblance of the magnetostriction along the  $c^*$  axis with the magnetization of the ladder.<sup>11</sup> This correspondence was already exploited in Ref. 14 to explain the three consecutive sign changes of the thermal expansion along  $c^*$ , that are observed at lowest temperatures as a function of magnetic field, in terms of entropy extrema.<sup>18</sup>

In addition, we analyzed the thermal expansion near the upper critical field  $H_{c2}$ . Sufficiently close to the quantum critical point at  $H_{c2}$ , the spin-ladder Hamiltonian (1.1) becomes equivalent to a model of free non-relativistic fermions with known microscopic parameters, see Sec. III A. This enables us to derive a parameter-free analytic formula for the thermal expansion along

the three crystallographic directions. At criticality,  $H = H_{c2}$ , we observe a  $1/\sqrt{T}$  divergence of thermal expansion down to our lowest temperatures. As we discussed in detail in Ref. 14, this strong singularity is rooted in the low dimensionality of the critical subsystem.

Finally, we predict a correction to the elastic moduli of  $(\text{C}_5\text{H}_{12}\text{N})_2\text{CuBr}_4$ , whose magnetic field and temperature dependence is governed by static four-spin correlation functions of the spin ladder. Typically, this correction is small, and it is indeed negligible for our analysis of magnetostriction in the measured temperature range. However, close to quantum criticality, the magnetic correction to the elastic moduli becomes proportional to the magnetic susceptibility  $\chi$ . As the susceptibility diverges at criticality as  $\chi \sim 1/\sqrt{T}$ , this should lead to a strong softening of the crystal rendering the elastic system in principle unstable at sufficiently low temperatures, see Sec. IIIB. We argued that this phenomenon is in fact generic for quantum critical systems if the strain couples to the square of the order parameter and, in addition, the criterion  $\nu(d+z) < 2$  is fulfilled. Our estimates show, however, that in  $(\text{C}_5\text{H}_{12}\text{N})_2\text{CuBr}_4$  this fluctuation induced first-order transition is not realized as the small inter-ladder coupling will cut-off the strong singularities before an instability can develop.

Whereas the strong singularity of  $\chi$  is particular to the quantum critical point of the spin ladder, a correction to the elastic tensor proportional to the magnetic susceptibility is a generic feature of magnetic-field driven quantum criticality. Such corrections have been observed in ultrasound experiments on  $\text{NH}_4\text{CuCl}_3$  by Schmidt *et al.*<sup>42</sup>

As an outlook, we remark that the precise knowledge of the magnetoelastic couplings of  $(\text{C}_5\text{H}_{12}\text{N})_2\text{CuBr}_4$  as given in Table I will be especially useful in the quest for a theoretical explanation of its thermal transport properties.<sup>45</sup>

### Acknowledgments

We acknowledge useful discussions with T. Giamarchi, J.A. Mydosh, K. Kiefer, A. Sologubenko, B. Thielemann, and M. Vojta. This work was supported by the Deutsche Forschungsgemeinschaft through Sonderforschungsbereich 608 and by the Swiss National Science Foundation. Computer time was allocated through the Swedish Grant No. SNIC 005/06-8.

- 
- <sup>1</sup> E. G. Batyev and L. S. Braginskii, Sov. Phys. JETP **60**, 781 (1984).
  - <sup>2</sup> T. Giamarchi, A.M. Tsvelik, Phys. Rev. B **59**, 11398 (1999).
  - <sup>3</sup> I. Affleck, Phys. Rev. B **41**, 6697 (1990).
  - <sup>4</sup> I. Affleck, Phys. Rev. B **43**, 3215 (1991).
  - <sup>5</sup> T. Giamarchi, Ch. Rüegg, and O. Tchernyshyov, Nature Phys. **4**, 198 (2008).
  - <sup>6</sup> Ch. Rüegg, N. Cavadini, A. Furrer, H.-U. Güdel, K. Krämer, H. Mutka, A. Wildes, K. Habicht, P. Vorderwisch, Nature **423**, 62 (2003).
  - <sup>7</sup> N. Johannsen, A. Vasiliev, A. Oosawa, H. Tanaka, and T. Lorenz, Phys. Rev. Lett. **95**, 017205 (2005).
  - <sup>8</sup> T. Lorenz, S. Stark, O. Heyer, N. Hollmann, A. Vasiliev, A. Oosawa, and H. Tanaka, J. Magn. Magn. Mat. **316**, 291 (2007).
  - <sup>9</sup> V.S. Zapf, D. Zocco, B.R. Hansen, M. Jaime, N. Harrison, C.D. Batista, M. Kenzelmann, C. Niedermayer, A. Lacerda, and A. Paduan-Filho, Phys. Rev. Lett. **96**, 077204 (2006).
  - <sup>10</sup> S.A. Zvyagin, J. Wosnitza, C.D. Batista, M. Tsukamoto, N. Kawashima, J. Krzystek, V.S. Zapf, M. Jaime, N.F. Oliveira Jr., and A. Paduan-Filho, Phys. Rev. Lett. **98**, 047205 (2007).
  - <sup>11</sup> B. C. Watson, V.N. Kotov, M.W. Meisel, D.W. Hall, G.E. Granroth, W.T. Montfrooij, S.E. Nagler, D.A. Jensen, R. Backov, M.A. Petruska, G.E. Fanucci, and D.R. Talham, Phys. Rev. Lett. **86**, 5168 (2001).
  - <sup>12</sup> V.O. Garlea, A. Zheludev, T. Masuda, H. Manaka, L.-P. Regnault, E. Ressouche, B. Grenier, J.-H. Chung, Y. Qiu, K. Habicht, K. Kiefer, and M. Boehm, Phys. Rev. Lett. **98**, 167202 (2007).
  - <sup>13</sup> H.J. Schulz, Phys. Rev. B **34**, 6372 (1986).
  - <sup>14</sup> T. Lorenz, O. Heyer, M. Garst, F. Anuso, A. Rosch, Ch. Rüegg, and K. Krämer, Phys. Rev. Lett. **100**, 067208 (2008).
  - <sup>15</sup> L. Zhu, M. Garst, A. Rosch, and Q. Si, Phys. Rev. Lett. **91**, 066404 (2003).
  - <sup>16</sup> R. KÜchler, N. Oeschler, P. Gegenwart, T. Cichorek, K. Neumaier, O. Tegus, C. Geibel, J. A. Mydosh, F. Steglich, L. Zhu, and Q. Si, Phys. Rev. Lett. **91**, 066405 (2003).
  - <sup>17</sup> S. Stark, O. Heyer, A. Vasiliev, A. Oosawa, H. Tanaka, and T. Lorenz, J. Mag. Mat. Mat. **310**, 1374 (2007).
  - <sup>18</sup> M. Garst and A. Rosch, Phys. Rev. B **72**, 205129 (2005).
  - <sup>19</sup> H. v. Löhneysen, A. Rosch, M. Vojta, and P. Wölfle, Rev. Mod. Phys. **79**, 1015 (2007).
  - <sup>20</sup> P. Gegenwart, Q. Si, F. Steglich, Nature Phys. **4**, 186 (2008).
  - <sup>21</sup> B. R. Patyal, B. L. Scott, and R. D. Willett, Phys. Rev. B **41**, 1657 (1990).
  - <sup>22</sup> Ch. Rüegg, B. Thielemann, K. Krämer, unpublished.
  - <sup>23</sup> L. D. Landau and E. M. Lifshitz, *Theory of Elasticity* (Butterworth-Heinemann, 1986).
  - <sup>24</sup> R. Chitra and T. Giamarchi, Phys. Rev. B **55**, 5816 (1997).
  - <sup>25</sup> F. D. M. Haldane, Phys. Rev. Lett. **50**, 1153 (1983).
  - <sup>26</sup> G. Chaboussant, M.-H. Julien, Y. Fagot-Revurat, M. Hanson, L. P. Lévy, C. Berthier, M. Horvatić, and O. Piovesana, Euro. Phys. J. B **6**, 167 (1998).
  - <sup>27</sup> F. Mila, Euro. Phys. J. B **6**, 201 (1998).
  - <sup>28</sup> K. Totsuka, Phys. Rev. B **57**, 3454 (1998).
  - <sup>29</sup> V.S. Zapf, V.F. Correa, P. Sengupta, C.D. Batista, M. Tsukamoto, N. Kawashima, P. Egan, C. Pantea, A. Migliori, J.B. Betts, M. Jaime, A. Paduan-Filho, arXiv:0705.0365.

- <sup>30</sup> O.F. Syljuasen, Phys. Rev. B **61**, R846 (2000).
- <sup>31</sup> M. Reigrotzki, H. Tsunetsugu, and T. M. Rice, J. Phys. C: Cond. Matt. **6**, 9325 (1994).
- <sup>32</sup> P.W. Anderson, Science **235**, 1196 (1987).
- <sup>33</sup> S. Sachdev, T. Senthil and R. Shankar, Phys. Rev. B **50** 258 (1994).
- <sup>34</sup> L. D. Landau and E. M. Lifshitz, *Statistical Physics* (Butterworth-Heinemann, 1984).
- <sup>35</sup> O. K. Rice, J. Chem. Phys. **22**, 1535 (1954).
- <sup>36</sup> C. Domb, J. Chem. Phys. **25**, 783 (1956).
- <sup>37</sup> A. I. Larkin and S. A. Pikin, JETP **29**, 891 (1969).
- <sup>38</sup> D. J. Bergman and B. I. Halperin, Phys. Rev. B **13**, 2146 (1976).
- <sup>39</sup> M. A. de Moura, T. C. Lubensky, Y. Imry, and A. Aharony, Phys. Rev. B **13**, 2176 (1976).
- <sup>40</sup> R. A. Cowley, Phys. Rev. B **13**, 4877 (1976).
- <sup>41</sup> E. Orignac, R. Citro, and T. Giamarchi, Phys. Rev. B **75**, 140403(R) (2007).
- <sup>42</sup> S. Schmidt, S. Zherlitsyn, B. Wolf, H. Schwenk, B. Lüthi, and H. Tanaka, Europhys. Lett. **53**, 591 (2001).
- <sup>43</sup> Ch. Rüegg, M. Oettli, J. Schefer, O. Zaharko, A. Furrer, H. Tanaka, K.W. Krämer, H.-U. Güdel, P. Vorderwisch, K. Habicht, T. Polinski, and M. Meissner, Phys. Rev. Lett. **93**, 037207 (2004).
- <sup>44</sup> M. Matsumoto, Phys. Rev. B **68**, 180403(R) (2003).
- <sup>45</sup> A. Sologubenko, T. Lorenz, A. Rosch, (in preparation).